Science of Remote Sensing 5 (2022) 100053

Contents lists available at ScienceDirect

Science of Remote Sensing

journal homepage: www.sciencedirect.com/journal/science-of-remote-sensing

Analysis of short-term soil moisture effects on the ASCAT backscatter-incidence angle dependence

Isabella Greimeister-Pfeil [a,b,*], Wolfgang Wagner [a,b], Raphael Quast [a], Sebastian Hahn [a], Susan Steele-Dunne [c], Mariette Vreugdenhil [a,b]

[a] Department of Geodesy and Geoinformation, Research Division Remote Sensing, TU Wien, Wiedner Hauptstraße 8-10, 1040, Vienna, Austria
[b] Centre for Water Resource Systems, TU Wien, Karlsplatz 13, 1040, Vienna, Austria
[c] Faculty of Civil Engineering and Geosciences, Delft University of Technology (TU Delft), Stevinweg 1, 2628, Delft, the Netherlands

ARTICLE INFO

Keywords:
Vegetation dynamics
Soil moisture
Vegetation optical depth
Advanced sScatterometer (ASCAT)
Microwave remote sensing
C-band

ABSTRACT

The incidence angle dependence of C-band backscatter is strongly affected by the presence of vegetation in the sensor footprint. Many studies have shown the suitability of this dependence for studying and monitoring vegetation dynamics. However, short-term dynamics in the backscatter-incidence angle dependence remain unexplained and indicate that secondary effects might be superimposed on the vegetation component. In this study, we hypothesize that the observed short-term dynamics are caused by soil moisture. We investigate the effect by exploring relationships between the slope of the backscatter-incidence angle dependence (σ') from the Advanced Scatterometer (ASCAT) and soil moisture, rainfall, temperature, and leaf area index. We carry out the analysis over six study regions in Portugal, Austria, and Russia with different climate, land cover, and vegetation cycles. Our results indicate that soil moisture has an effect on σ'. Spearman correlations of σ' anomalies with soil moisture anomalies are stronger than with any other variable in most study regions and range from -0.38 to -0.70. Even when accounting for effects of water on canopy, correlations between σ' and soil moisture remain relatively strong, ranging from -0.14 to -0.46. These results confirm the presence of secondary effects in the dynamic σ', which need to be corrected for when applying σ' in studies of vegetation dynamics. A correction may be achieved by the application of a suitable smoothing on σ' (i.e., removing high frequency signal components), by masking observations taken under wet conditions, or by the use of models that explicitly account for the effect of soil moisture on σ'.

1. Introduction

Earth observation using active and passive microwave sensors has a long tradition in the context of environmental research. Over land, these sensors show high sensitivity to changes in the soil and vegetation water content, surface roughness, vegetation structure, and, in the case of passive sensors, temperature. As opposed to optical radiation, microwaves can penetrate cloud cover and are independent of daylight. The first microwave missions were launched in the 1970s and 80s. Since then, they have provided global, continuous estimates of a variety of biogeophysical variables such as soil moisture (Wagner et al., 2013; Dorigo et al., 2017; Al Bitar et al., 2017; Chan et al., 2018; Bauer-Marschallinger et al., 2018), rainfall (Brocca et al., 2017), above-ground biomass (Santoro et al., 2015; Saatchi et al., 2007; Bousquet et al., 2021), plant water content (Konings et al., 2019), and gross primary production (Teubner et al., 2018). Microwave observations have further been successfully applied for the estimation of vegetation optical depth (VOD) (Owe et al., 2008; Liu et al., 2011; Konings et al., 2016; Vreugdenhil et al., 2016) and the monitoring of vegetation dynamics (Frappart et al., 2020), the study of interactions between soil moisture and climate (Seneviratne et al., 2010), and in the context of food security (Karthikeyan et al., 2020). These studies have proven the suitability and multiple benefits provided by microwave observation systems. In light of climate change, the availability of high quality, reliable, and easily accessible data will be even more critical in order to study and understand its various impacts on the environment. This entails the constant development and assessment of algorithms and underlying assumptions, particularly with the availability of new missions with improved spatial,

* Corresponding author. Department of Geodesy and Geoinformation, Research Division Remote Sensing, TU Wien, Wiedner Hauptstraße 8-10, 1040, Vienna, Austria.
E-mail address: isabella.pfeil@geo.tuwien.ac.at (I. Greimeister-Pfeil).

https://doi.org/10.1016/j.srs.2022.100053
Received 6 January 2022; Received in revised form 12 April 2022; Accepted 21 April 2022
Available online 26 April 2022

temporal, and radiometric resolutions.

In active microwave remote sensing, the characteristic interactions between the radar beam and the land surface lead to different scattering mechanisms. Over bare soil, surface roughness and soil water content cause diffuse scattering of the radar beam at the boundary between the atmosphere and the land surface. Over vegetation, volume scattering in the canopy is the dominant scattering mechanism and controlled by canopy structure and water content. In addition, sudden changes in the canopy structure, e.g., over cropland and deciduous forest, may trigger specific scattering mechanisms and affect the observed radar signal. In the context of remote sensing of vegetation using scatterometers, the scattering characteristics of a vegetation canopy are exploited. In particular, the dependence of the observed backscatter values (σ^0) on the incidence angle (θ) has been found to carry valuable information (Wagner et al., 1999a). This dependence can be retrieved if (almost) simultaneous backscatter observations from different incidence angles are available for a target area, such as provided by the scatterometers onboard of the European Remote Sensing satellites (ERS-1, ERS-2) and their successor, the Advanced Scatterometer (ASCAT) onboard the series of Metop satellites. Wagner et al. (1999b) used the observation geometry of ERS to model the vegetation component (vc) in the backscatter signal based on the slope (σ') and curvature (σ'') of the backscatter-incidence angle dependence. Several studies confirmed a connection between σ' and vegetation dynamics and advanced the understanding of the underlying processes. Vreugdenhil et al. (2016) used a water cloud model to convert the long-term average σ' to VOD, a measure of the optical thickness of a canopy related to vegetation water content and structure, leaf area index (LAI), and biomass. Steele-Dunne et al. (2019) analyzed dynamic σ' time series over the North American prairie and showed the negative impact of a long dryspell on grasslands. Pfeil et al. (2020) carried out a detailed study of the effect of spring reactivation in deciduous broadleaf forest on σ'.

Furthermore, Wagner et al. (1999b) used vc for disentangling the vegetation and soil moisture (SM) components in the ERS backscatter signal. They applied vc in order to correct for vegetation dynamics and retrieve SM using a semi-empirical change detection method (Wagner et al., 1999a, 1999c). Since then, the approach has been developed further for ASCAT onboard the series of Metop satellites launched in 2006, 2012 and 2018 (Naeimi et al., 2009). From their exploratory analysis of the ERS-1/-2 scatterometers, Wagner et al. (1999b) concluded that a SM effect on σ' and σ'' is weak or nonexistent. Therefore, they assumed that SM effects on σ' and σ'' can, in a first approximation, be neglected. This assumption has become part of the core postulates of the TU Wien SM retrieval algorithm (Wagner et al., 1999c; Vreugdenhil et al., 2016; Hahn et al., 2020).

Traditionally, vc has been modelled as a climatology (vc_{clim}), i.e., σ' and σ'' are modelled for every day of year. However, vegetation dynamics can vary significantly in different years due to meteorological conditions, and vc_{clim} is thus expected to be outperformed by a dynamic vegetation correction (vc_{dyn}) when used for the retrieval of SM (Vreugdenhil et al., 2016). Melzer (2013) showed how σ'_{dyn} and σ''_{dyn} can be modelled in a robust way. The use of this vc_{dyn} for SM retrieval from ASCAT has been evaluated in different studies with mixed outcomes: Pfeil et al. (2018) analyzed the differences in ASCAT SM time series when using vc_{dyn} as opposed to vc_{clim} in an agricultural catchment in Austria. They found that the correspondence with in-situ SM does not improve significantly, contradicting the expectation. Steele-Dunne et al. (2021) analyzed ASCAT SM retrieved with vc_{clim} and vc_{dyn} over the United States. They concluded that the application of vc_{dyn} leads to improvements in the resulting SM dataset over regions with a temporal trend or changes in the amplitude or timing of phenological processes, but not in general, due to short-term variability in σ'_{dyn}.

Short-term dynamics in the order of several days to a few weeks in σ'_{dyn} have not been studied in detail. As vegetation growth processes usually take place on temporal scales of several weeks, it is likely that the observed short-term effects are in fact secondary effects superimposed on the vegetation signal at the coarse spatial resolution of ASCAT. A possible explanation was put forward by Quast and Wagner (2016), who used radiative transfer theory to model backscatter from the land surface. They found that, in contrast to the assumption made in (Wagner et al., 1999b), σ' and σ'' might in fact be significantly affected by SM. A recent study by Vermunt et al. (2021) found that interception and dew, i.e., water present on the canopy (WOC), impact L-band backscatter. In a follow-on study (Khabbazan et al., 2022), the authors demonstrated that interception and dew influenced retrievals of vegetation parameters. It is likely that this effect also plays a role, or is even stronger, in C-band microwave remote sensing as the wavelength is shorter and closer to the size of plant constituents.

The aim of this study is to advance the understanding of short-term variability in σ'_{dyn} and in particular the investigation of a potential SM effect on σ'. Whereas reference data for SM can be readily obtained from multiple sources, e.g., based on remote sensing data, land surface models, or data assimilation products, the availability of WOC reference data is currently limited to dedicated field experiments. Thus, we account for WOC only indirectly by masking potentially affected observations. As the effects are expected to be more pronounced on σ' than on its derivative, σ'', and the estimate of σ'' is less robust than the estimate of σ', we will not look at σ'' in this study. The main challenge of this investigation is that SM, WOC, and vegetation dynamics are closely related through the water, energy and carbon cycles, and disentangling the effects needs a careful analysis. Thus, we base the study on different types of analyses and aim at answering the following questions:

1. How do σ'_{clim} and σ'_{dyn} differ, and can we relate the differences to SM or LAI dynamics?
2. What are the correlations between anomalies of σ'_{dyn}, SM, rainfall, temperature, and LAI?
3. Is there a direct relationship between SM and the daily slope values, the so-called local slopes σ'_{local}?
4. Do SM variations explain short-term dynamics in σ'_{dyn} even when excluding observations potentially affected by WOC?
5. What is the magnitude of a potential SM effect on σ'_{dyn}?

The calculation of σ'_{local}, σ'_{dyn}, and σ'_{clim} will be described in section 3.1. Section 5 provides details on each analysis step, including the chosen WOC masking approach. We carry out the analysis for six regions in Austria, Portugal and Russia, which differ in climate, land cover, and the factors that limit vegetation growth.

2. Vegetation, soil moisture and roughness effects on σ'

An observed backscatter value (σ^0) is affected by the characteristics of the land surface in the sensor footprint, and by the different scattering mechanisms that are activated. This, in turn, is primarily controlled by the sensor's frequency and polarization, and the incidence angle of the observation (Ulaby, 1981). Fig. 1 shows a generalized overview of different effects that contribute to σ^0. In the case of bare soil, the radiation is reflected on the surface, and with increasing surface roughness, a larger part of the radiation is scattered back to the sensor. If a surface appears rough or smooth to a scatterometer is defined by the size of the surface height variations, the wavelength of the radar beam, and the incidence angle. In general, σ^0 is higher over rough surfaces and decreases with increasing incidence angle. This decrease with increasing incidence angle is stronger for smooth surfaces. In addition, the soil water content plays a fundamental role in microwave remote sensing, as wet soil increases σ^0 due to its high dielectric constant and consequently higher scattering strength. As opposed to bare soil, a vegetation canopy appears as an inhomogeneous medium with a higher penetration depth, and thus acts like a volume scatterer, which scatters the incident

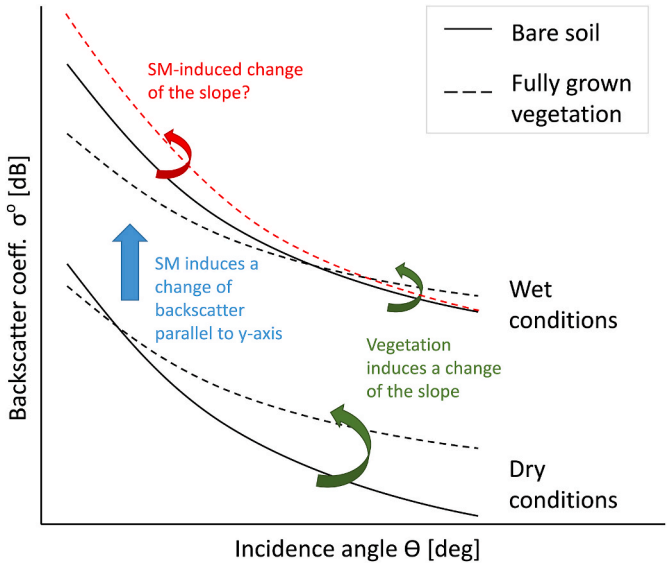

Fig. 1. Dependence of the backscatter coefficient on the incidence angle under dry and wet conditions, for bare soil and fully grown vegetation (after (Wagner et al., 1999b)). The hypothesized change of σ' due to SM variations is shown in red. (For interpretation of the references to colour in this figure legend, the reader is referred to the Web version of this article.)

radiation diffusely in all directions. In this case, the backscattered radiation fraction depends less on the incidence angle. In addition to surface and volume scattering, double-bounce backscattering between vegetation constituents and the (soil or water) surface might occur. Double-bounce scattering is typical for flooded vegetation, e.g., paddy fields, but may also play an important role over croplands with predominantly vertically oriented plant constituents when observed with sensors that operate in vertical polarization mode. With increasing incidence angle, i.e., a longer pathway through the vegetation and thus decreasing canopy transmissivity, double-bounce effects are expected to become weaker (Xu et al., 2019). In most regions, except for, e.g., tropical rainforests or desert areas, the sensor footprint often covers a mixture of different land cover types, which also develop differently throughout the growing season. Thus, σ^0, as well as the sensitivity of σ^0 to the incidence angle of the observation (σ'), are usually affected by both surface and volume (and in some cases, double-bounce) scattering, and change over the year based on SM and vegetation conditions. Thereby, the presence of vegetation in the sensor footprint and the increase of vegetation water content and biomass during the growing season reduce the sensitivity to SM.

As stated in the introduction, recent studies suggest that the SM-induced increase of absolute backscatter might not be consistent across all incidence angles. As the attenuation of the radar beam by a vegetation canopy is higher at large incidence angles due to longer paths through the canopy, an increase in SM might increase σ^0 (expressed in dB) observed at low incidence angles more than at high incidence angles, leading to a steeper, i.e., more negative, σ'. This hypothesized process is shown in red in Fig. 1. This would mean that σ' changes due to vegetation dynamics (rather long-term changes) as well as due to SM dynamics (rather short-term changes of a few days to weeks).

3. Datasets

Since SM and vegetation growth are closely connected through the water, carbon and energy cycles, we compare σ' not only to SM but also to LAI, rainfall, and surface temperature. LAI, representing vegetation growth and dynamics, is obtained from the Copernicus Global Land Service (CGLS). Surface temperature, as a proxy for photosynthesis and land-atmosphere exchanges in radiation- or temperature-limited areas, and rainfall data are obtained from the ECMWF Re-Analysis (ERA5-Land). An overview of the datasets is given in Table 1. We collected data from all datasets for the period 2007–2019. Timestamps with a surface temperature below 3 °C or snow cover above 10% have been masked. Unless stated otherwise, we use time series that have been smoothed with a 42-day rolling Epanechnikov kernel in order to match the TU Wien change detection σ' calculation (see section 3.1). This smoothing preserves the seasonal cycle as well as short-term events of several days to weeks, but removes events of shorter time scales, i.e., a few days or below. In the case of ASCAT, the Epanechnikov kernel is applied in order to obtain a robust estimation of σ'. Therefore, the observations are weighted based on their relative distance (d) to a given day using the following equation:

$$weight = 0.75*(1 - d^2) \quad (1)$$

Both absolute and anomaly time series are used in this study. Anomalies are calculated by subtracting the long-term average (2007–2019) from the absolute values. The long-term average is obtained by applying a 5-day smoothing window on the time series (gap filling and short-term event correction), calculating the mean value for each day of year based on data from all available years, and applying a 30-day smoothing window on the resulting time series (long-term event correction). The long-term average thus represents the average annual seasonal cycle, without variations in the order of several days to weeks. The anomaly time series on the other hand contain only these short-term deviations from the long-term average, i.e., without a seasonal cycle.

3.1. Advanced Scatterometer (ASCAT)

We test our hypothesis using σ^0 observations and thereof derived σ' from the Advanced Scatterometer (ASCAT). ASCAT is a side-looking C-band radar onboard the Metop-A, -B, and –C satellites, which were launched in 2006, 2012, and 2018, respectively. Recently, Metop-A has reached its end, and was deorbited in November 2021. ASCAT observes the surface with a frequency of $f = 5.255$ GHz across an incidence angle range of 25°–53° (mid-beam) and 34°– to 64° (fore- and aft-beams), and provides vertically co-polarized (VV) σ^0.

The description of the backscatter-incidence angle dependence, i.e. σ' and σ'', has been investigated in many studies. Please note that as stated in the introduction, we focus only on σ' in this study. Wagner et al. (1999b) estimated σ' based on all backscatter observations from a certain period of the year (slope climatology, σ'_{clim}). Later, Melzer (2013) showed that σ' can be derived for sliding time windows of a few weeks (dynamic slope, σ'_{dyn}). Hahn et al. (2017) compared σ'_{clim} and σ'_{dyn} and showed the robustness of the σ'_{dyn} calculation on a global scale. All these studies used backscatter observations from ASCAT or its predecessors, the scatterometers onboard the ERS-1 and -2 satellites (ESCAT). The calculation of both σ'_{clim} and σ'_{dyn} is based on the so-called local slopes, which can be derived from the (almost) simultaneous observations of the fore- (f), mid- (m) and aft-beams (a) provided by ESCAT and ASCAT:

Table 1
Overview of datasets.

Variable	Unit	Dataset	Spatial sampling
σ^0	dB	ASCAT	12.5 km
σ'_{clim}, σ'_{dyn}, σ'_{local}	dB/deg	ASCAT	12.5 km
Rainfall	m/h	ERA5-Land	9 km
Soil moisture (0–7 cm depth)	m^3m^{-3}	ERA5-Land	9 km
Surface temperature	$°C$	ERA5-Land	9 km
Leaf area index	[–]	SPOT-VGT, PROBA-V	resamp. to ASCAT grid

$$\sigma'_{mf} = \frac{\sigma^0_m - \sigma^0_f}{\theta_m - \theta_f}, \quad \sigma'_{ma} = \frac{\sigma^0_m - \sigma^0_a}{\theta_m - \theta_a} \tag{2}$$

$$\theta_{mf} = \frac{\theta_m - \theta_f}{2}, \quad \theta_{ma} = \frac{\theta_m - \theta_a}{2} \tag{3}$$

where σ^0 denotes the backscatter, θ is the incidence angle, and σ'_{mf} and σ'_{ma} are the local slopes (σ'_{local}). The dynamic slope, σ'_{dyn}, is estimated for every day by calculating a linear regression based on all σ'_{local} values within a window of ±21 days, weighted by their temporal distance from the respective date using a rolling Epanechnikov kernel. The result of this linear regression are σ'_{dyn} and σ''_{dyn} of the respective date. The estimation of σ'_{clim} (and σ''_{clim}) is done in the same way, but using all observations from a certain period of all available years. In this study, we applied the same methods for the estimation of σ'_{local}, σ'_{clim}, and σ'_{dyn}, i.e., descriptions of the linear part of the backscatter-incidence angle dependence on different temporal scales.

σ' is generally exploited in three ways: First, it is used to normalize backscatter observations to any desired incidence angle. Second, σ' is used to correct for vegetation effects and the subsequently reduced sensitivity to SM in the TU Wien SM retrieval algorithm. Third, it is used to calculate VOD from ASCAT (Vreugdenhil et al., 2016) and for the study of vegetation dynamics (Steele-Dunne et al., 2019; Pfeil et al., 2020). The main assumption underlying the latter two uses is that σ' is only affected by vegetation water content and structure, not by SM conditions (or other secondary effects). The assumption is based on early studies by Wagner et al. (1999b) who calculated differences between measured σ'_{local} and their first-order approximation and compared the variability of these differences for grassland, boreal forest, and peri-alpine forest regions. High variability in these differences would indicate the presence of natural short-term changes in σ'. They found the variability to be similar among the vegetation regions, although backscatter from forested areas is much more stable than the backscatter from grassland, and concluded that σ' is generally not affected by short-term changes of environmental conditions. Thus, they also expected correlations between σ' and SM to be weak. This study was based on ESCAT data from two years (1993 and 1994). Nowadays, backscatter samples are available for much longer periods and at higher spatial, temporal, and radiometric resolutions. It is thus possible to revisit and potentially update the interpretation by Wagner et al. (1999b).

3.2. CGLS leaf area index

The Copernicus Global Land Service (CGLS) provides LAI from the SPOT-VGT and PROBA-V sensors (Camacho et al., 2013; Dierckx et al., 2014). In this study, version 2 of the dataset was used, which is available from 1999–June 2020 and has a spatial resolution of 1 km. The LAI data was spatially resampled to the scale of ASCAT by averaging over all 1 km pixels within a 0.09° radius around the center of the respective ASCAT grid point.

3.3. ERA5-land

Hourly SM, rainfall, and surface temperature were obtained from the ERA5-Land dataset (Mu ñ oz Sabater, 2019) and resampled to daily averages. Surface temperature was included in the study to account for the fact that land-atmosphere exchanges are radiation- and/or temperature-limited in some regions. All time series used in this study were masked for cold and frozen conditions using daily surface temperatures (masked if temperature is below 3 °C), and for snow cover (masked if snow content is greater than 10%).

3.4. CCI land cover

The dominant, i.e., most frequent land cover class for each ASCAT grid point has been derived from the CCI land cover dataset version v2.0.7, year 2015 (ESA, 2017).

4. Study area

We selected six regions of interest (ROIs) in Austria, Portugal and Russia in order to study SM and vegetation effects on σ' under different environmental conditions. These six regions have different dominant climate regimes, land cover types, and vegetation cycles. Table 2 provides an overview of the study regions, and the factors mainly limiting vegetation growth (estimated from (Nemani et al., 2003), Fig. 1a). Long-term average annual temperature, SM, and LAI are shown in Fig. 2 in order to illustrate differences of climate and vegetation growth between the ROIs. Note that short-term variations in the order of days to weeks are filtered out during the calculation of the long-term average. Average temperatures in Austria range from slightly below 0 °C in winter to around 20 °C in the summer months. SM is relatively constant throughout the year, with lowest values during the warm summer months. As shown by LAI, the growing season in cropland starts in March, peaks in June and ends around late September. In grassland, the peak of the growing season also happens around June, with a less sharp decline afterwards until autumn. In evergreen needleleaf forest, LAI increases constantly from around March to July and then decreases again until the end of autumn. The development is similar in Russia. However, LAI is lower there due to the sparse vegetation cover. Average temperatures range from around −30 °C to 10 °C. In these four ROIs, vegetation growth is mainly limited by radiation and temperature. In Portugal on the other hand, vegetation growth is mainly water-limited. Average annual temperatures range from around 10 °C to above 20 °C. In summer, SM levels become very low. The peak of the growing season occurs around May/June, before the SM level reaches its minimum (around 0.15 m^3/m^3).

Fig. 3 shows the average σ'_{dyn} time series for each ROI. Characteristic seasonal vegetation cycles, similar to LAI in Fig. 2, can be identified. In addition, interannual variability due to different weather conditions is clearly visible in all ROIs. σ'_{dyn} is most dynamic over cropland, varying from below −0.15 dB/deg to −0.05 dB/deg. Lowest slope dynamics are observed over evergreen needleleaf forest, with slope values from around −0.10 dB/deg to −0.075 dB/deg. The steepest slopes are observed over sparse vegetation in Russia, where the average slope in the short growing season is around −0.15 dB/deg.

5. Methods

5.1. Correlation analysis - seasonal dynamics

In a first step, we analyze the seasonal dynamics of the climatology slope (σ'_{clim}) and the dynamic slope (σ'_{dyn}) by correlating the time series with LAI and SM (smoothed with a 42-day rolling window). If the short-term variations in σ'_{dyn} represent vegetation dynamics, we expect to see similar dynamics in LAI, and thus a strong correlation between LAI and σ'_{dyn}. On the other hand, if the short-term dynamics are caused by SM, the correlation between SM and σ'_{dyn} will be stronger than between SM and σ'_{clim}, and the correlation between LAI and σ'_{dyn} will be weaker than between LAI and σ'_{clim}. Please note that we are not primarily interested in absolute correlations here, as the seasonal cycle in all variables will lead to high correlation values without necessarily bearing causality (Papagiannopoulou et al., 2017). Instead, we only look at the relative differences in the correlations of LAI and SM with σ'_{clim} and σ'_{dyn}. We use Spearman's rank correlation coefficient, as the variables might be

Table 2
Abbreviation, Koeppen-Geiger climate class, factors limiting vegetation growth (LVG), number of grid points (n), and center coordinates for the six regions of interest.

Region	Abbreviation	Climate	LVG	n	Center
Austria (cropland)	AT_cr	Dfb	radiation	79	16.14°E, 48.33°N
Austria (grassland)	AT_gr	Cfb, Dfb	radiation	23	13.84°E, 48.12°N
Austria (evergreen needleleaf forest)	AT_nf	Dfb,c, ET	radiation, temperature	86	14.90°E, 47.11°N
Portugal (tree, shrub mosaic)	PT_ts	Csb	radiation, water	93	7.46°W, 41.00°N
Portugal (cropland)	PT_cr	Csa	water	80	7.82°W, 38.37°N
Russia (sparse vegetation)	RU_sv	Dfc	temperature, radiation	102	108.20°E, 72.00°N

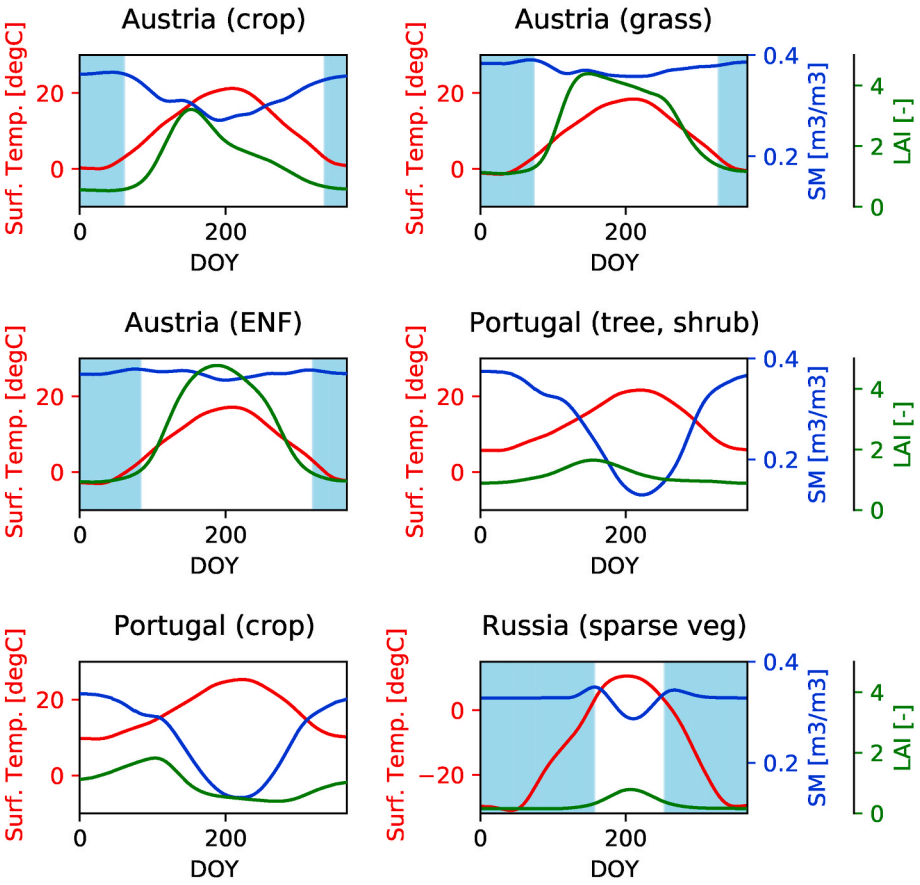

Fig. 2. Long-term average annual temperature, SM and LAI for every day of year (DOY). Periods where the average temperature is less than or equal to 3 °C are shown in light blue. Please note the different temperature axis for Russia. (For interpretation of the references to colour in this figure legend, the reader is referred to the Web version of this article.)

non-linearly related.

5.2. Correlation analysis - anomalies

Next, we carry out a correlation analysis on anomaly time series, i.e., time series where the long-term seasonal cycle has been subtracted. As mentioned above, this is critical in the case of variables with a strong seasonal cycle, as potential (non-)correlations in the short-term dynamics of the variables will always be outweighed by long-term similarities. In this step, we also include rainfall and temperature anomalies in addition to SM and LAI, as short-term vegetation dynamics might rather be reflected (indirectly) in these variables than in LAI. In addition, we carry out a multiple linear regression (MLR) in order to test the explanatory power of anomalies of the individual variables, as well as combinations thereof, on dynamics in σ'_{dyn}. The explanatory power is given by the coefficient of determination, R^2, and is calculated using the ordinary least squares (OLS) function of the *statsmodels* Python package.

5.3. Local slopes analysis

As described in section 3.1, σ'_{dyn} is based on the weighted σ'_{local} values of all observations within a ±21-day window. Thus, potential short-term effects of SM are reduced in σ'_{dyn} (as well as in σ'_{clim}), but much more pronounced in σ'_{local}. In the presented analysis, the uncertainty in the local slopes is reduced by averaging the local slope pairs:

$$\sigma'_{\mathrm{local}} = \frac{\sigma'_{\mathrm{mf}} + \sigma'_{\mathrm{ma}}}{2}, \quad \theta_{\mathrm{local}} = \frac{\theta_{\mathrm{mf}} + \theta_{\mathrm{ma}}}{2} \tag{4}$$

We look at changes of the observed σ'_{local} and compare them to the corresponding changes in SM. For this purpose, we use the SM value from the timestamp closest to the ASCAT observation, as opposed to the 42-day smoothed values that were used before. In case of a SM effect on the slope, we expect the slope to become steeper as SM increases. As σ'_{local} is calculated for each observation, the values are not yet normalized for incidence angle effects. Thus, this analysis is carried out per incidence angle (rounded to full integers). We do a visual analysis of the σ'_{local}

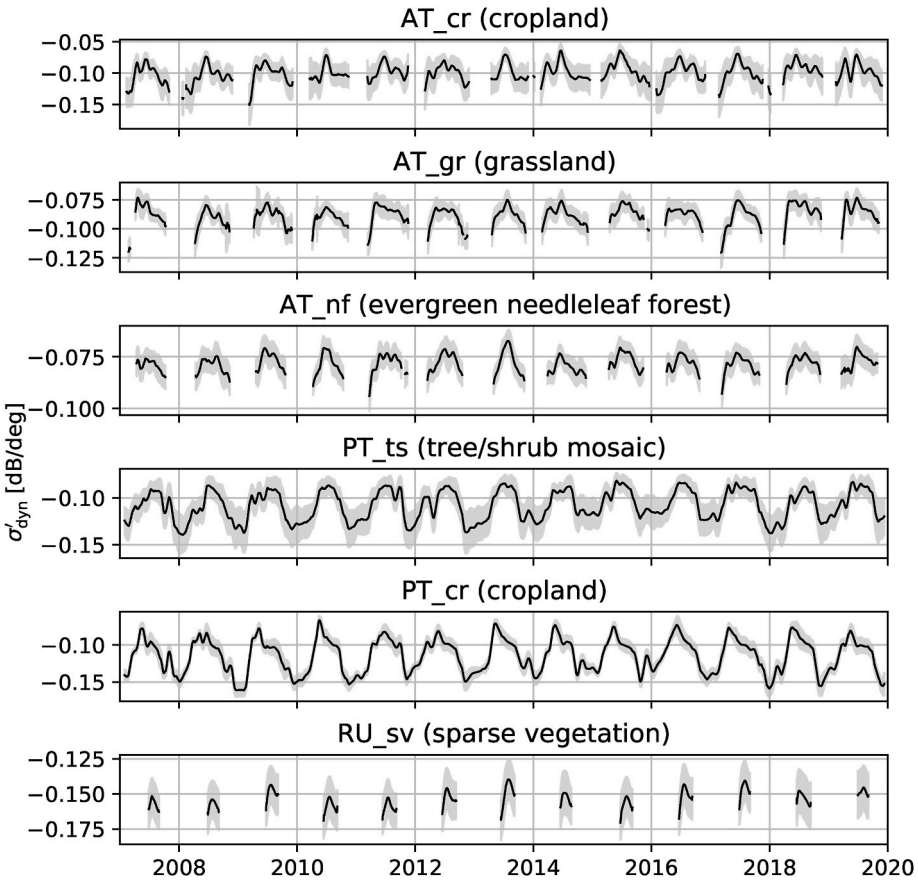

Fig. 3. Average σ'_{dyn} time series for each ROI (black). The grey shaded area shows the ±1 standard deviation range within each ROI.

dynamics during and after rainfall events in order to support the discrimination of SM and vegetation effects in σ'_{local} and, subsequently, σ'_{dyn}.

5.4. Indirect assessment of WOC effects on the ASCAT slope

A recent study by Vermunt et al. (2021) using L-band backscatter suggested that water on canopy (WOC), due to, e.g., interception and dew, may affect the backscatter significantly. It is assumed that C-band σ^0 and σ' are also strongly affected by WOC. However, these effects are poorly understood, and it is not known how ASCAT's sensitivity to SM changes when WOC is present. In order to investigate correlations between σ' and SM and at the same time reduce the uncertainty with respect to WOC, we apply an indirect WOC masking: First, we identify all σ'_{local} observed on days with rainfall (maximum rainfall value greater than 1 mm/h) and remove these observations. Moreover, we exclude all observations from morning overpasses (before 10:00 a.m.m), as dew is expected to occur mainly in the morning hours. Just like in the previous sections, we then derive the σ'_{dyn} time series based on all remaining σ'_{local} values within a ±21-day window. This modified σ'_{dyn} is referred to as $\sigma'_{dyn,nWOC}$ ("dynamic slope, no water on canopy"). The assumption that we take here is that a potential WOC effect on the slope lasts shorter than a SM effect, as the drying of the leaves happens more quickly than the decrease in SM. The proposed approach is not expected to provide a perfect masking of WOC. For example, WOC may persist for a longer duration depending on weather conditions and leaf structure. Nonetheless, in the absence of reference data for WOC, the proposed masking is adopted as a meaningful indirect indicator of WOC. It also has to be noted that the estimation of $\sigma'_{dyn,nWOC}$ is less robust than the original σ'_{dyn} due to the reduced number of σ'_{local}.

Similar as in section 5.3, SM, σ'_{local}, σ'_{dyn} and $\sigma'_{dyn,nWOC}$ are visually compared to each other and analyzed for selected grid points. Then, we redo the correlation analysis from section 5.2 with $\sigma'_{dyn,nWOC}$ and compare the results with the correlations obtained with σ'_{dyn}.

5.5. Quantification of SM effects on the ASCAT slope

Finally, we provide an estimate of the magnitude of SM effects on σ'_{dyn} by calculating linear regressions between anomalies of 42-day smoothed SM and σ'_{dyn}. The regression line is used to obtain the change in σ'_{dyn} at the largest positive (wet) SM anomaly that occurred in each ROI. Then, the order of magnitude of the change in σ'_{dyn} is related to the characteristic σ'_{dyn} dynamics in each ROI.

6. Results

6.1. Correlation analysis - seasonal dynamics

Fig. 4 shows example time series of σ'_{clim}, σ'_{dyn}, SM, and LAI for a grid point in Marchfeld, an agricultural region in eastern Austria. All four variables show a characteristic seasonal cycle and inter-annual variations, e.g., lower maximum values in σ'_{dyn} and LAI in 2017, 2018, and 2019, and short-term variations in σ'_{dyn} and SM. As can be seen in the figure, some of the short-term variations in σ'_{dyn} correspond to variations in SM, but not to LAI, which shows relatively smooth temporal dynamics apart from inter-annual variations in the absolute values. For this grid point, the Spearman correlations between σ'_{clim} and SM, and σ'_{clim} and

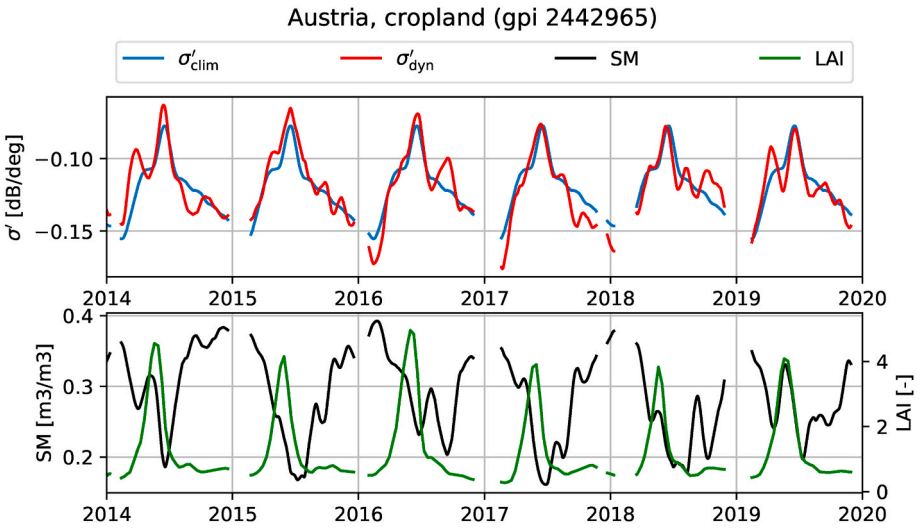

Fig. 4. σ'_{clim}, σ'_{dyn}, SM and LAI for a grid point in AT_cr (lon: 16.79°, lat: 48.62°).

LAI are −0.53 and 0.86, respectively. The correlations of SM and LAI with σ'_{dyn} are −0.72 and 0.70, i.e., the correlation between SM and σ'_{dyn} is −0.19 lower (stronger) than with σ'_{clim}, whereas it is 0.16 lower (weaker) for LAI and σ'_{dyn} than LAI and σ'_{clim}. We calculated these correlations for all grid points in the six ROIs and found a consistent behavior (Fig. 5): for all ROIs, the median correlation between SM and σ'_{dyn} is stronger than between SM and σ'_{clim}, whereas the opposite is true for LAI, except for the PT_cr ROI, where the correlation between σ'_{clim} and LAI is slightly lower. The weak correlations in PT_cr can be explained by a relatively quick drop in LAI in early summer, which in most years corresponds to the timing of the shallowest slope, but after the peak, the slope values decrease more gradually. An example of this behavior is shown in Fig. 6 for a grid point in Portugal dominated by non-irrigated arable land. Figs. 4 and 6 also show that there is a small time lag between σ' and LAI, which is due to a sensitivity to different biophysical parameters: whereas LAI is a representation of the photosynthetically active leaf area per surface area, σ' is sensitive to the vegetation density, water content, and vegetation structure. These time lags are typically of a few weeks and have been observed for σ' (Pfeil et al., 2018) and the closely related VOD (Jones et al., 2011) (see Fig. 7).

6.2. Correlation analysis - anomalies

In a next step, we calculated Spearman correlations between anomaly time series, i.e., time series where the long-term seasonal cycle has been removed. Table 3 shows the median correlation for each ROI. For all ROIs except PT_cr, the correlation is strongest between σ'_{dyn} and SM, ranging from −0.37 to −0.70. For PT_cr, the correlation is strongest between σ'_{dyn} and rainfall (−0.51), but also relatively high between σ'_{dyn} and SM (−0.45). The correlations with LAI range from −0.14 to 0.26 and are thus much weaker than with SM and rainfall. As shown in section 6.1, LAI does not show large short-term dynamics, and inter-annual variations mainly show in the absolute values and the long-term development of LAI throughout the growing season. The correlations with temperature anomalies range from 0.23 to 0.43, which most likely reflects the close relationship between temperature and SM, i.e., drying of the soil with higher temperatures and evaporation rates. The fact that the σ'_{dyn} correlations with rainfall and SM are higher than with temperature suggests that the short-term dynamics in σ'_{dyn} do not represent temperature-induced vegetation dynamics, e.g., by an increased water demand from the atmosphere leading to water uptake by the leaves, but more likely a direct SM effect.

The OLS analysis has the advantage that also multivariate relationships can be tested. The R^2 coefficient represents the percentage of variation in the σ'_{dyn} anomalies that can be explained by another variable or combinations thereof (Fig. 7). LAI has been excluded here because of the weak correlations with slope anomalies as shown in Table 3. In general, similar results are obtained as presented above. SM is in all regions the most important variable for explaining short-term dynamics in σ'_{dyn}. Over cropland and sparse vegetation, rainfall has a higher R^2

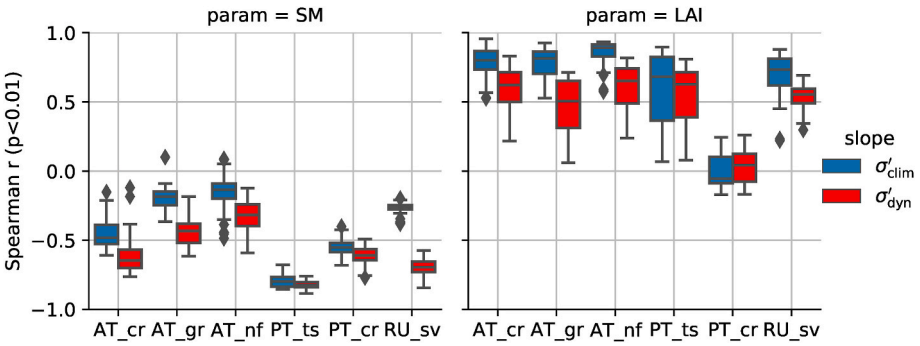

Fig. 5. Spearman correlation coefficient (r) of σ'_{clim} and σ'_{dyn} with SM and LAI, for each ROI. Only grid points with a significant correlation ($p < 0.01$) are included. The boxes show the quartiles, and the whiskers show the rest of the distribution. The horizontal line inside the boxes shows the median value. Outliers are shown by diamonds.

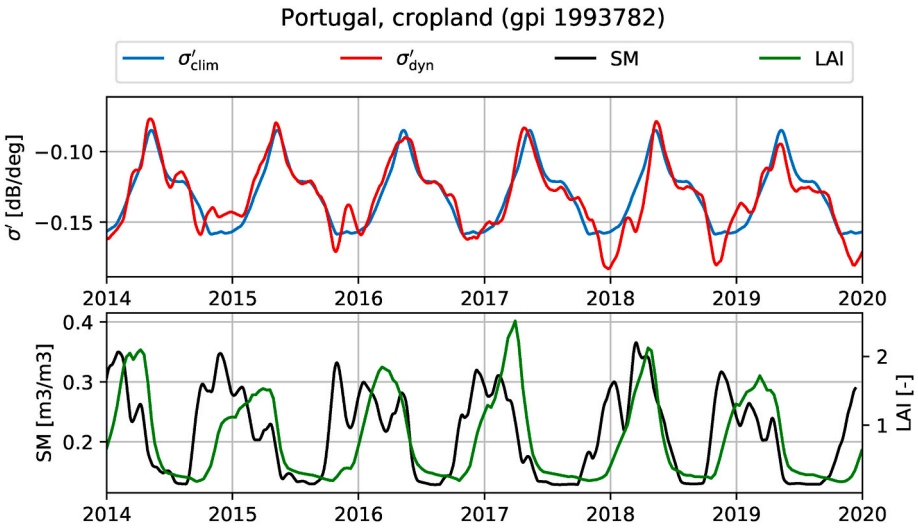

Fig. 6. σ'_{clim}, σ'_{dyn}, SM and LAI for a grid point in PT_cr (lon: -8.09°, lat: 37.82°).

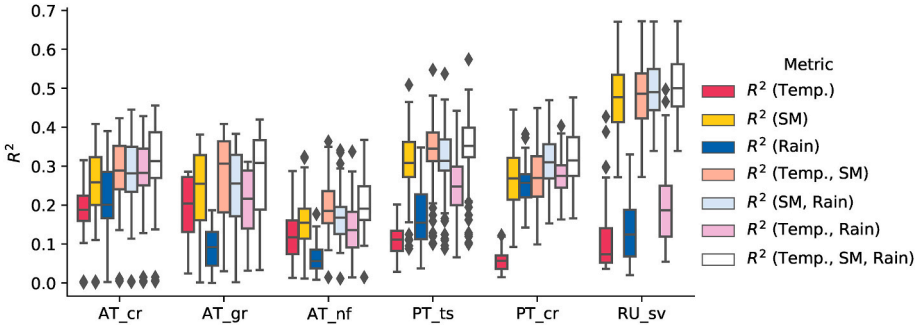

Fig. 7. Coefficient of determination (R^2) obtained for regressions of temperature, soil moisture, rainfall, and combinations thereof against σ'_{dyn}, for each ROI. The boxes show the quartiles, and the whiskers show the rest of the distribution. The horizontal line inside the boxes shows the median value. Outliers are shown by diamonds.

Table 3
Median Spearman correlation (significant at p<0.01) between anomalies of σ'_{dyn} and the given variable. The maximum absolute correlation is given in bold.

Region	Rainfall	Soil moisture	Temperature	LAI
AT_cr	−0.49	**−0.52**	0.43	−0.07
AT_gr	−0.34	**−0.51**	0.41	−0.14
AT_nf	−0.24	**−0.37**	0.35	0.10
PT_ts	−0.44	**−0.52**	0.32	0.10
PT_cr	**−0.51**	−0.45	0.23	0.13
RU_sv	−0.32	**−0.70**	0.27	0.26

coefficient than temperature, whereas the opposite is true in grassland, needleleaf forest and shrubland. In all ROIs, the highest R^2 coefficients are obtained when combining temperature, SM and rainfall anomalies. In all regions except AT_cr, where the combined R^2 values are very similar, a clear drop in R^2 is observed when including only temperature and rainfall in the analysis. Overall, the highest R^2 values are obtained in RU_sv, with median values above 0.50 and maximum values around 0.70. Vegetation growth in this ROI is generally limited by temperature and radiation, not by SM availability. The fact that much higher correlations between σ'_{dyn} and SM than temperature are observed supports again the hypothesis that the short-term dynamics in σ'_{dyn} can be explained by SM dynamics to a very large extent. R^2 is lowest over needleleaf forest, indicating that there, the bare soil scattering component is largely attenuated by the canopy, and subsequently, the SM effect is lower.

6.3. Local slopes analysis

The local slopes σ'_{local} allow for the analysis of a potential SM effect at a much finer temporal scale. We selected two grid points as examples for the detailed study of a relationship between SM and short-term dynamics in σ'_{local} and σ'_{dyn}. Fig. 8 shows σ'_{local} observed over a range of incidence angles, the 42-day smoothed σ'_{dyn} time series, and ERA5-Land SM, temporally matched to σ'_{local}, for a grid point in AT_cr (left) and PT_cr (right). Displayed are only σ'_{local} values from the incidence angle with most observations in the bins 25°–35°, 35°–45°, 45°–55° and 55°–65°, whereas the resulting 42-day smoothed σ'_{dyn} (shown in black) includes all observations from the entire incidence angle range. The shown time series are from 2014, as interesting SM and σ'_{dyn} dynamics occurred in this year in AT_cr and PT_cr.

In the first example (AT_cr), SM was relatively high in April and May 2014, and decreased relatively smoothly in June. In the beginning of July, SM increased again. As opposed to SM, σ'_{local} and the resulting σ'_{dyn} started to increase (become more shallow) in March, then decreased during the period of higher SM in April and May, increased in June, and quickly decreased at the beginning of July. From August onwards, SM stayed constantly high. σ'_{local} and σ'_{dyn} decreased, mainly reflecting the end of the growing season and senescence of the vegetation, but also

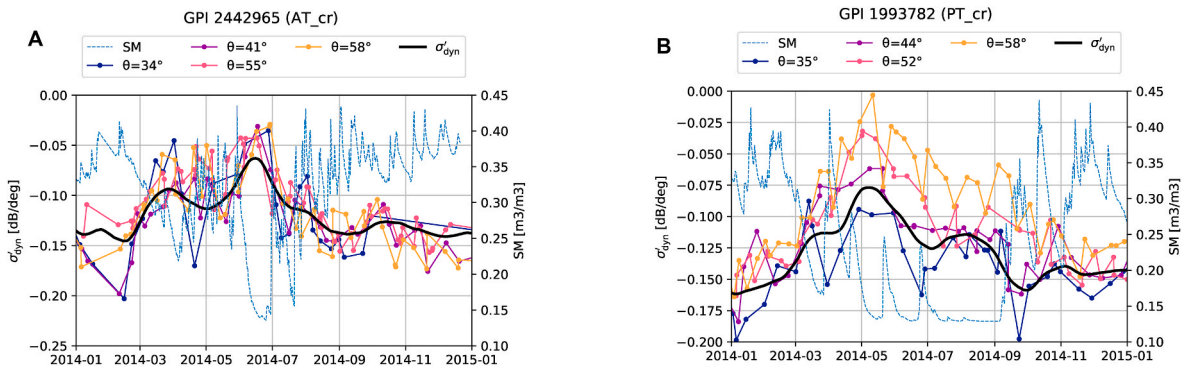

Fig. 8. Soil moisture (SM), σ'_{local} from the five most frequent incidence angles and σ'_{dyn} for a grid point in (left) AT_cr and (right) PT_cr.

including some short-term effects such as in October and the beginning of November, where again, the σ'_{local} and also σ'_{dyn} dynamics are clearly opposed to SM dynamics. In the second example (PT_cr), SM was high in the winter months in 2014, decreased from March onwards and increased again in September, interrupted by a number of SM increases and rapid decreases due to rainfall events. The distinct SM dynamics are also found in σ'_{local}: whenever SM increased, σ'_{local} decreased. The effect seems particularly pronounced at lower incidence angles, for example when comparing the $\sigma'_{local}(\theta = 35°)$ time series with $\sigma'_{local}(\theta = 58°)$. The time series also show the dependence on the overpass timing: the large rainfall event in mid-May is reflected in $\sigma'_{local}(\theta = 58°)$, but missed by $\sigma'_{local}(\theta = 35°)$. In σ'_{dyn}, the short-term effects that are so clearly visible in σ'_{local} appear smoothed, but can still be linked to large rainfall events for example in the beginning of April, the end of June and the beginning of September. Again, the seasonal dynamics are dominated by the vegetation cycle. These observations indicate that rainfall events and thus SM increases steepen σ'_{dyn} where a flattening is expected as a result of growing vegetation. Similarly, at the end of the growing season, the steepening of σ'_{dyn} is exacerbated by SM increases.

6.4. Indirect assessment of WOC effects on the ASCAT slope

In section 6.2, we showed that short-term σ'_{dyn} anomalies are highly correlated with SM and rainfall. However, rainfall has no direct effect on backscatter. Rather, it is SM and WOC after rainfall events (and, in the morning hours, WOC in the form of dew) that affect backscatter. Similar to SM, WOC might have an impact on σ'. However, due to a lack of reference data for WOC, we can currently assess contributions of WOC only indirectly. As described in section 5.4, we do this by removing measurements potentially affected by WOC before the σ'_{dyn} calculation. Fig. 9 shows the remaining σ'_{local}, the original σ'_{dyn}, the new $\sigma'_{dyn,nWOC}$ with measurements from rainy days and morning overpasses removed, and SM, temporally matched to the dates of the remaining σ'_{local} values.

Compared to Fig. 8, the AT_cr example (left panel) shows a longer slope increase in spring, but again a decrease around the beginning of May, when SM is high. In autumn, σ'_{dyn} and $\sigma'_{dyn,nWOC}$ are very similar. In the PT_cr example (right panel), the number of quick drops in the $\sigma'_{local}(\theta = 58°)$ time series is reduced. Remaining short-term effects are mainly visible during the large SM increase around the beginning of April and at the beginning of July, when the vegetation is already beginning senescence. The resulting $\sigma'_{dyn,nWOC}$ dynamics are very similar to the original σ'_{dyn}. The reduced robustness of the calculation of $\sigma'_{dyn,nWOC}$ shows for example in November 2014.

This analysis shows that when excluding measurements from rainy days and morning overpasses, some short-term dynamics in σ'_{local} are indeed removed, which may be related to WOC. However, the main dynamics in σ' are still present, as the 42-day smoothed $\sigma'_{dyn,nWOC}$ does not differ much from σ'_{dyn}. This suggests that WOC might play a (significant) role, however, it represents only another influence on σ'_{dyn}, in addition to the SM effect.

To quantify the relative importance of the SM effect on σ'_{dyn} with respect to the WOC effect, we repeat the correlation analysis from section 6.2, now using $\sigma'_{dyn,nWOC}$ instead of σ'_{dyn}. Because of the only indirect effect on rainfall and the fact that we used rainfall to correct for WOC in $\sigma'_{dyn,nWOC}$, we omit this variable here. Table 4 shows the median Spearman correlations between anomalies of SM, temperature, and LAI and $\sigma'_{dyn,nWOC}$ (r). In addition, the differences between the absolute correlations calculated between the explanatory variables and $\sigma'_{dyn,nWOC}$ and the absolute correlations calculated between the explanatory variables and σ'_{dyn} (section 6.2, Table 3) are given ($\Delta abs(r)$). A boxplot of the correlations between anomalies of SM, σ'_{dyn}, and $\sigma'_{dyn,nWOC}$ is shown in Fig. 10. Both Table 4 and Fig. 10 show that for all ROIs, the correlations between $\sigma'_{dyn,nWOC}$ and SM are lower, but still significant, and higher than with temperature or LAI. The correlations are mainly reduced in

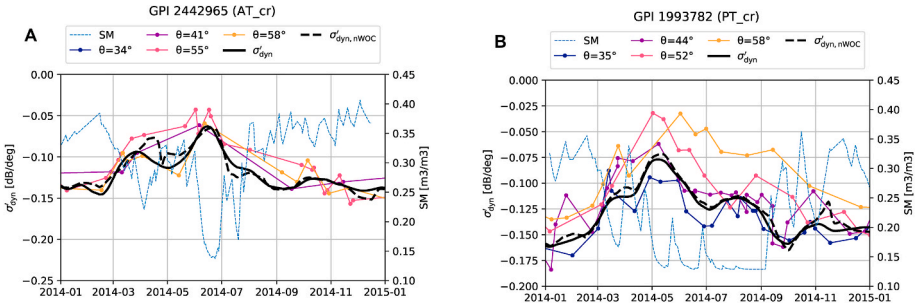

Fig. 9. Same as Fig. 8, but without σ'_{local} from rainy days and morning overpasses, and the resulting $\sigma'_{dyn,nWOC}$ in addition (dashed black line) to the original σ'_{dyn}.

Table 4
Median Spearman correlation (significant at p<0.01) between anomalies of $\sigma'_{dyn,nWOC}$ and the given variable (r), and the difference to the correlations with σ'_{dyn} shown in Table 3 ($\Delta abs(r)$; calculated between absolute r values). The maximum absolute correlation is given in bold.

Region	Soil moisture		Temperature		LAI	
	r	$\Delta abs(r)$	r	$\Delta abs(r)$	r	$\Delta abs(r)$
AT_cr	**−0.36**	−0.16	0.28	−0.15	0.05	−0.02
AT_gr	**−0.24**	−0.27	0.19	−0.22	−0.08	−0.06
AT_nf	**−0.12**	−0.25	0.12	−0.23	0.10	0.00
PT_ts	**−0.45**	−0.07	0.27	−0.05	0.07	−0.03
PT_cr	**−0.42**	−0.03	0.18	−0.05	0.10	−0.03
RU_sv	**−0.46**	−0.24	0.21	−0.06	0.17	−0.09

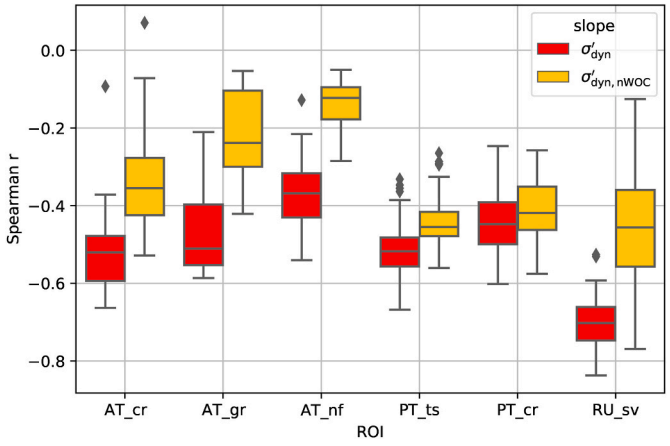

Fig. 10. Median Spearman correlation (significant at p<0.01) between anomalies of SM and σ'_{dyn} (red) and between anomalies of SM and $\sigma'_{dyn,nWOC}$ (yellow). The boxes show the quartiles, and the whiskers show the rest of the distribution. The horizontal line inside the boxes shows the median value. Outliers are shown by diamonds. (For interpretation of the references to colour in this figure legend, the reader is referred to the Web version of this article.)

ROIs with higher rainfalls, i.e., Austria and Russia, showing that masking observations from rainy days and morning overpasses effectively reduces the impact of WOC (and SM, to a certain extent). These results suggest that we need to find a way to also fully reduce the SM effect in $\sigma'_{dyn,nWOC}$ in order to obtain a σ'_{dyn} that mainly includes vegetation water content and structure effects.

6.5. Quantification of SM effects on the ASCAT slope

As the previous sections indicate that SM causes secondary, short-term dynamics in σ'_{dyn}, we will give an estimate of the magnitude of the effect. Please note that in this estimation, we assume that SM causes all short-term effects in σ'_{dyn}, neglecting other effects which are, e.g., related to the vegetation structure. We do not correct for WOC here, as $\sigma'_{dyn,nWOC}$ is less robust than σ'_{dyn}, and we do not have reference data for the actual presence and amount of WOC. The calculations are done for the maximum observed wet anomaly (i.e., 42-day smoothed SM anomalies) during the study period. The results should thus be interpreted as maximum values, and smaller SM effects are expected for most of the time. In order to quantify the SM effect, we calculate linear regressions between anomalies of 42-day smoothed SM and σ'_{dyn}. Fig. 11 shows the median regression lines for each ROI along with values from a randomly selected subset of grid points. Boxplots of the linear regression slope (k) and R^2 values for the ROIs are shown in Fig. 12. The k values are similar in most ROIs, and range from around −0.20 to −0.05 dB/deg per m^3/m^3. AT_nf sticks out as the k values are slightly higher there, i.e., the regression line is flatter (median $k = -0.08$). The lowest median k are found in AT_gr and RU_sv (−0.14). Using k, the magnitude of the SM effect with respect to the seasonal cycle of σ'_{dyn} can be quantified: For example, in AT_cr, the largest positive (wet), 42-day smoothed SM anomaly from 2007 to 2019 was 0.10 m^3/m^3 (SM_{wet}). With a median k in AT_cr of −0.13 dB/deg per m^3/m^3, SM_{wet} corresponds to an effect on σ'_{dyn} of −0.013 dB/deg. Typically, σ'_{dyn} ranges from −0.15 dB/deg to −0.06 dB/deg in cropland, i.e., over the year, the change in σ'_{dyn} is 0.09 dB/deg. The value of −0.013 dB/deg thus corresponds to 0.013/0.09 = 14.4% of the average, total seasonal variation of σ'_{dyn}. Table 5 gives an overview of the median values for k and the 95% confidence interval (k_{min} and k_{max}), the maximum SM anomaly during 2007–2019, minimum and maximum σ'_{dyn}, the difference between maximum and minimum σ'_{dyn} ($\Delta\sigma'_{dyn}$), and the thereof derived effect of the maximum wet anomaly on the slope, for each ROI. The SM effect is lowest, but still considerable, in AT_nf (6%). This is followed by grassland (AT_gr) with an effect of 11.2%. Over cropland (AT_cr and PT_cr), the effect is of 14.4% and 13.0%, respectively. The largest effects are observed over tree and shrub mosaic (PT_ts) and sparse vegetation (RU_sv), with 17.3% and 23.3%. The SM effect thus increases with decreasing vegetation density, as with sparser vegetation, the signal is more and more coming from the soil. As stated above, these numbers are expected to be lower during most of the time. Still, they indicate that σ'_{dyn} is not just related to

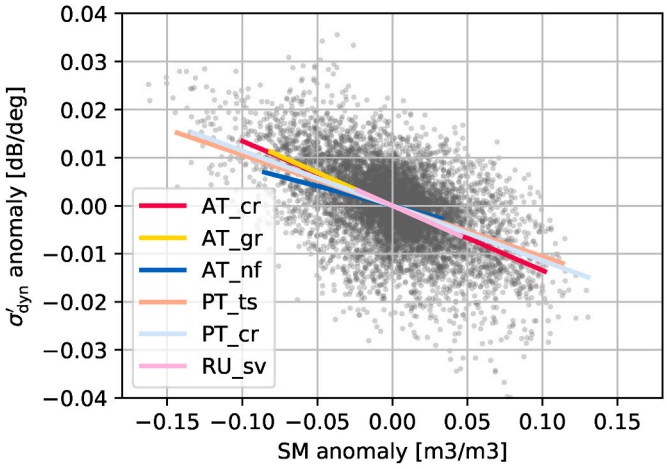

Fig. 11. Scatter plot of SM and σ'_{dyn} anomalies from randomly selected grid points for each ROI, along with the linear regression lines (calculated from all grid points of each ROI).

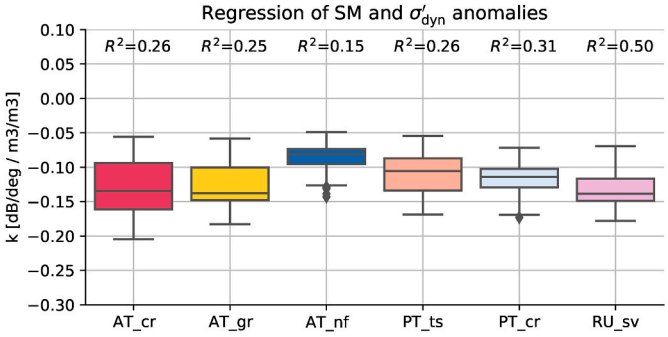

Fig. 12. Linear regression slope k of SM and σ'_{dyn} anomalies for each ROI. The boxes show the quartiles, and the whiskers show the rest of the distribution. The horizontal line inside the boxes shows the median value. Outliers are shown by diamonds. R^2 values of the linear regressions are shown above each box.

Table 5
Quantification of the SM effect on σ'_{dyn} k is the median slope of the linear regression between anomalies in SM and σ'_{dyn}. 95% of k are within k_{min} and k_{max}. The largest positive SM anomaly, SM_{wet}, is given in m^3/m^3; $\sigma'_{dyn,min}$, $\sigma'_{dyn,max}$ and $\Delta\sigma'_{dyn}$ are given in dB/deg. The SM effect has been calculated based on the ROI-specific median values of all parameters.

ROI	k_{min}	k	k_{max}	SM_{wet}	$\sigma'_{dyn,min}$	$\sigma'_{dyn,max}$	$\Delta\sigma'_{dyn}$	Effect
AT_cr	−0.14	−0.13	−0.13	0.10	−0.15	−0.06	0.09	14.4%
AT_gr	−0.14	−0.14	−0.13	0.04	−0.12	−0.07	0.05	11.2%
AT_nf	−0.09	−0.08	−0.07	0.03	−0.10	−0.06	0.04	6.0%
PT_ts	−0.11	−0.11	−0.10	0.11	−0.15	−0.08	0.07	17.3%
PT_cr	−0.12	−0.11	−0.11	0.13	−0.17	−0.06	0.11	13.0%
RU_sv	−0.15	−0.14	−0.13	0.05	−0.17	−0.14	0.03	23.3%

vegetation dynamics but also notably affected by SM. The secondary short-term dynamics caused by SM may be as large as a fifth of the seasonal, vegetation-induced variation in σ'_{dyn}.

7. Discussion

Backscatter measured by active microwave sensors is affected by multiple factors. Due to the coarse spatial resolution, each measurement usually contains signals from multiple land cover types. Moreover, rainfall, SM, temperature, and vegetation dynamics are closely related, which makes it especially difficult to separate the effects in the observed backscatter values. We tried to overcome these challenges by including different types of analyses, which all point to the same result: SM causes high-frequency variability in σ', which appears as a secondary effect on top of the dominant vegetation signal. The effect can be explained by an SM-induced increase of the backscatter coefficient over vegetation canopies that still allow a fraction of the radiation to penetrate through and reach the surface. As vegetation canopies are less transparent at high incidence angles due to longer paths through the canopy, observations from lower incidence angles are more affected than observations from higher incidence angles. Consequently, the slope of the backscatter-incidence angle dependence becomes steeper, even though the vegetation canopy did not change. The assumption that SM causes an equal increase of σ^0 (when expressed in dB) across all incidence angles is thus not strictly fulfilled. Rather, SM might increase σ^0 especially at low incidence angles and thus lead to a steeper σ', as displayed in red in Fig. 1. We gave a rough magnitude estimate of the SM effect, showing that it can be as high as one fifth of the total seasonal variation in σ'_{dyn}. The separation of vegetation, SM, and WOC effects on σ'_{dyn} as well as their respective contributions should be investigated further using more complex approaches, e.g., empirical orthogonal function analysis.

Despite the clear results, we would like to discuss potential shortcomings of our analysis in the following.

We carried out all our analyses on full time series, i.e., covering all months from January to December, apart from a masking of days with temperatures below 3 °C and snow cover. We did not do any seasonal split of the data because we were interested in the general presence of an SM effect. Single seasons might however show slightly different results. For example, we know of phenological processes such as spring reactivation in deciduous broadleaf forest that can impact σ' during a certain time of the year. These are neglected here, and it is assumed that all short-term effects have the same causes and appear throughout the year.

As a reference for vegetation dynamics, we use LAI in this study. However, LAI is a suitable, but not perfect reference for VOD, which σ' is most closely related to (Grant et al., 2016). For example, time lags have been observed between LAI and VOD (Jones et al., 2011; El Hajj et al., 2019). These time lags are frequency-dependent and expected to be smaller for C-band (Grant et al., 2016; El Hajj et al., 2019). In the presented study, we tested the use of lagged correlations, but, as the time lags were small for all ROIs except for PT_cr and did not affect the results and conclusions of the study, they were omitted. Another way to overcome this problem might be to compare σ' to VOD derived from passive microwave sensors, which are expected to be less susceptible to SM effects because passive retrievals of SM and VOD make less strong pre-assumptions. However, also passive retrievals of VOD are associated with uncertainties, for example, due to radio frequency interference and pixel heterogeneity (Li et al., 2021; Bousquet et al., 2021).

The impact of WOC on total backscatter and the relative contributions of the various scattering mechanisms are still poorly understood. Without reference data on how the presence of WOC alters the sensitivity to surface SM, it is difficult to disentangle the respective impacts on the backscatter return. It is however expected that WOC leads to increased backscatter, while at the same time reducing the sensitivity to surface SM. The WOC filtering applied in this study can thus not be used to identify WOC directly, but should be interpreted as a method to mask events where both WOC as well as an increase in SM lead to secondary effects on σ'_{dyn} that do not originate from vegetation dynamics. Note that the examples discussed in sections 6.3 and 6.4 had a rather low number of rainfall events in 2014. In regions and years with more frequent rainfall events, removing WOC-affected measurements drastically reduces the number of σ'_{local}, leading to highly unstable σ'_{dyn} estimates in some cases. The effective removal of WOC and SM effects for the estimation of σ'_{dyn} will thus require very thorough investigation.

In the operational TU Wien SM retrieval algorithm, the estimation of the seasonal vegetation cycle is based on observations from several years and thus, short-term effects of SM become irrelevant. This explains the good performance of the operational ASCAT SM product as shown in many studies (Al-Yaari et al., 2014; Pierdicca et al., 2015; Miyaoka et al., 2017; Chen et al., 2018; Mousa and Shu, 2020; Hahn et al., 2020). Our findings provide an explanation for studies (Pfeil et al., 2018; Steele-Dunne et al., 2021) that did not find an improvement in the accuracy of SM datasets when retrieving them with vc_{dyn} instead of vc_{clim}. In order to benefit from an ASCAT-derived vc_{dyn} in the SM retrieval and in studies of vegetation dynamics, all SM effects must first be corrected in the signal. A solution might be the application of a suitable temporal smoothing on σ' in order to reduce SM effects in the signal while still keeping interannual vegetation dynamics. Other approaches could be the masking of observations taken under wet conditions, such as applied for WOC in this study, or by the use of models that explicitly account for the effect of soil moisture on σ'.

8. Conclusions

In this study, we revisited the assumption that soil moisture has a negligible effect on the slope σ' of the backscatter-incidence angle dependence. Based on this assumption, σ' has been used in studies of vegetation dynamics, for the retrieval of VOD, and to model the vegetation component in the backscatter signal. However, recent studies indicated that a soil moisture contribution may be present in the slope of the backscatter-incidence angle dependence. We analyzed this potential soil moisture effect on σ' by comparing σ', rainfall, soil moisture, temperature, and leaf area index time series over six study regions with different climate, land cover, and vegetation cycles. The obtained results lead us to the following conclusions:

- The slope of the backscatter-incidence angle dependence is dominated by the vegetation cycle, but is affected by soil moisture at short temporal scales. This SM effect can be larger than 20% of the seasonal, vegetation-induced variation over sparse vegetation. Over dense vegetation, the observed effect is lower (6% in evergreen needleleaf forest).
- Short-term secondary effects are mitigated when using a climatology slope (σ'_{clim}) due to long-term averaging. The use of σ'_{clim} is however only suitable for applications that do not look at interannual vegetation dynamics.
- As the slope has been found to be a useful complement to optical datasets for vegetation studies (Petchiappan et al., 2021), short-term secondary effects should be further investigated and a robust method for their mitigation should be developed.

The findings from this study advance the understanding of vegetation and soil moisture effects on active microwave observations. The study also showed that there is a need to better understand interactions between C-band microwaves and water on canopy, i.e., how water on canopy alters σ^0 and σ', and how it affects the sensitivity to soil moisture.

Author contributions

Conceptualization, I.G.-P. and W.W.; methodology, I.G.-P., W.W., M. V., S.H., S.S.-D., R.Q.; investigation, I.G.-P.; visualization, I.G.-P.; writing—original draft preparation, I.G.-P.; writing—review and editing, all authors. All authors have read and agreed to the published version of the manuscript.

Funding

This research was co-funded by the Austrian Space Application Program (Daily Water Cycle Radar project, Grant Number: 873658) and the European Organisation for the Exploitation of Meteorological Satellites (EUMETSAT) Satellite Application Facility on Support to Operational Hydrology and Water Management (H SAF). Mariette Vreugdenhil was supported by ESA's Living Planet Fellowship SHRED (contract number 4000125441/18/I-NS). The authors acknowledge TU Wien Bibliothek for financial support through its Open Access Funding Programme.

Declaration of competing interest

None.

Acknowledgements

ERA5-Land hourly data (Mu ñ oz Sabater, 2019) was downloaded from the Copernicus Climate Change Service (C3S) Climate Data Store. The results contain modified Copernicus Climate Change Service information 2020. Neither the European Commission nor ECMWF is responsible for any use that may be made of the Copernicus information or data it contains.

References

Al Bitar, A., Mialon, A., Kerr, Y.H., Cabot, F., Richaume, P., Jacquette, E., Quesney, A., Mahmoodi, A., Tarot, S., Parrens, M., Al-Yaari, A., Pellarin, T., Rodriguez-Fernandez, N., Wigneron, J.-P., 2017. The global SMOS level 3 daily soil moisture and brightness temperature maps. Earth Syst. Sci. Data 9, 293–315.

Al-Yaari, A., Wigneron, J.-P., Ducharne, A., Kerr, Y.H., Wagner, W., De Lannoy, G., Reichle, R., Al Bitar, A., Dorigo, W., Richaume, P., et al., 2014. Global-scale comparison of passive (smos) and active (ascat) satellite based microwave soil moisture retrievals with soil moisture simulations (merra-land). Rem. Sens. Environ. 152, 614–626.

Bauer-Marschallinger, B., Freeman, V., Cao, S., Paulik, C., Schaufler, S., Stachl, T., Modanesi, S., Massari, C., Ciabatta, L., Brocca, L., et al., 2018. Toward global soil moisture monitoring with sentinel-1: harnessing assets and overcoming obstacles. IEEE Trans. Geosci. Rem. Sens. 57, 520–539.

Bousquet, E., Mialon, A., Rodriguez-Fernandez, N., Prigent, C., Wagner, F.H., Kerr, Y.H., 2021. Influence of surface water variations on vod and biomass estimates from passive microwave sensors. Rem. Sens. Environ. 257, 112345.

Brocca, L., Crow, W.T., Ciabatta, L., Massari, C., De Rosnay, P., Enenkel, M., Hahn, S., Amarnath, G., Camici, S., Tarpanelli, A., et al., 2017. A review of the applications of ascat soil moisture products. IEEE J. Sel. Top. Appl. Earth Obs. Rem. Sens. 10, 2285–2306.

Camacho, F., Cernicharo, J., Lacaze, R., Baret, F., Weiss, M., 2013. Geov1: lai, fapar essential climate variables and fcover global time series capitalizing over existing products. part 2: validation and intercomparison with reference products. Rem. Sens. Environ. 137, 310–329.

Chan, S.K., Bindlish, R., O'Neill, P., Jackson, T., Njoku, E., Dunbar, S., Chaubell, J., Piepmeier, J., Yueh, S., Entekhabi, D., et al., 2018. Development and assessment of the SMAP enhanced passive soil moisture product. Rem. Sens. Environ. 204, 931–941.

Chen, F., Crow, W.T., Bindlish, R., Colliander, A., Burgin, M.S., Asanuma, J., Aida, K., 2018. Global-scale evaluation of smap, smos and ascat soil moisture products using triple collocation. Rem. Sens. Environ. 214, 1–13.

Dierckx, W., Sterckx, S., Benhadj, I., Livens, S., Duhoux, G., Van Achteren, T., Francois, M., Mellab, K., Saint, G., 2014. Proba-v mission for global vegetation monitoring: standard products and image quality. Int. J. Rem. Sens. 35, 2589–2614.

Dorigo, W., Wagner, W., Albergel, C., Albrecht, F., Balsamo, G., Brocca, L., Chung, D., Ertl, M., Forkel, M., Gruber, A., et al., 2017. ESA CCI soil moisture for improved earth system understanding: state-of-the art and future directions. Rem. Sens. Environ. 203, 185–215.

El Hajj, M., Baghdadi, N., Wigneron, J.-P., Zribi, M., Albergel, C., Calvet, J.-C., Fayad, I., 2019. First vegetation optical depth mapping from sentinel-1 c-band sar data over crop fields. Rem. Sens. 11, 2769.

Esa, 2017. Land cover cci product user guide version 2. Tech. Rep 2017. Available at: maps.elie.ucl.ac.be/CCI/viewer/download/ESACCI-LC-Ph2-PUGv2_2.0.pdf.

Frappart, F., Wigneron, J.-P., Li, X., Liu, X., Al-Yaari, A., Fan, L., Wang, M., Moisy, C., Le Masson, E., Aoulad Lafkih, Z., et al., 2020. Global monitoring of the vegetation dynamics from the vegetation optical depth (VOD): a review. Rem. Sens. 12, 2915.

Grant, J., Wigneron, J.-P., De Jeu, R., Lawrence, H., Mialon, A., Richaume, P., Al Bitar, A., Drusch, M., Van Marle, M., Kerr, Y., 2016. Comparison of smos and amsr-e vegetation optical depth to four modis-based vegetation indices. Rem. Sens. Environ. 172, 87–100.

Hahn, S., Reimer, C., Vreugdenhil, M., Melzer, T., Wagner, W., 2017. Dynamic characterization of the incidence angle dependence of backscatter using metop ascat. IEEE J. Sel. Top. Appl. Earth Obs. Rem. Sens. 10, 2348–2359.

Hahn, S., Wagner, W., Steele-Dunne, S.C., Vreugdenhil, M., Melzer, T., 2020. Improving ascat soil moisture retrievals with an enhanced spatially variable vegetation parameterization. IEEE Trans. Geosci. Rem. Sens.

Jones, M.O., Jones, L.A., Kimball, J.S., McDonald, K.C., 2011. Satellite passive microwave remote sensing for monitoring global land surface phenology. Rem. Sens. Environ. 115, 1102–1114.

Karthikeyan, L., Chawla, I., Mishra, A.K., 2020. A review of remote sensing applications in agriculture for food security: crop growth and yield, irrigation, and crop losses. J. Hydrol. 586, 124905.

Khabbazan, S., Steele-Dunne, S., Vermunt, P., Judge, J., Vreugdenhil, M., Gao, G., 2022. The influence of surface canopy water on the relationship between l-band backscatter and biophysical variables in agricultural monitoring. Rem. Sens. Environ. 268, 112789.

Konings, A.G., Piles, M., Rötzer, K., McColl, K.A., Chan, S.K., Entekhabi, D., 2016. Vegetation optical depth and scattering albedo retrieval using time series of dual-polarized l-band radiometer observations. Rem. Sens. Environ. 172, 178–189.

Konings, A.G., Rao, K., Steele-Dunne, S.C., 2019. Macro to micro: microwave remote sensing of plant water content for physiology and ecology. New Phytol. 223, 1166–1172.

Li, X., Wigneron, J.-P., Frappart, F., Fan, L., Ciais, P., Fensholt, R., Entekhabi, D., Brandt, M., Konings, A.G., Liu, X., et al., 2021. Global-scale assessment and inter-comparison of recently developed/reprocessed microwave satellite vegetation optical depth products. Rem. Sens. Environ. 253, 112208.

Liu, Y.Y., De Jeu, R.A., McCabe, M.F., Evans, J.P., Van Dijk, A.I., 2011. Global long-term passive microwave satellite-based retrievals of vegetation optical depth. Geophys. Res. Lett. 38.

Melzer, T., 2013. Vegetation modelling in warp 6.0. In: Proceedings of the EUMETSAT Meteorological Satellite Conference, pp. 16–20. Vienna, Austria.

Miyaoka, K., Gruber, A., Ticconi, F., Hahn, S., Wagner, W., Figa-Saldana, J., Anderson, C., 2017. Triple collocation analysis of soil moisture from metop-a ascat and smos against jra-55 and era-interim. IEEE J. Sel. Top. Appl. Earth Obs. Rem. Sens. 10, 2274–2284.

Mousa, B., Shu, H., 2020. Spatial evaluation and assimilation of smap, smos, and ascat satellite soil moisture products over africa using statistical techniques. Earth Space Sci. 7, e2019EA000841.

Muñoz Sabater, J., 2019. Era5-land hourly data from 1981 to present, copernicus climate change service (c3s) climate data store (cds). https://doi.org/10.24381/cds.e2161bac accessed on 28-sep-2020.

Naeimi, V., Bartalis, Z., Wagner, W., 2009. Ascat soil moisture: an assessment of the data quality and consistency with the ers scatterometer heritage. J. Hydrometeorol. 10, 555–563.

Nemani, R.R., Keeling, C.D., Hashimoto, H., Jolly, W.M., Piper, S.C., Tucker, C.J., Myneni, R.B., Running, S.W., 2003. Climate-driven increases in global terrestrial net primary production from 1982 to 1999. Science 300, 1560–1563.

Owe, M., de Jeu, R., Holmes, T., 2008. Multisensor historical climatology of satellite-derived global land surface moisture. J. Geophys. Res.: Earth Surf. 113.

Papagiannopoulou, C., Miralles, D.G., Decubber, S., Demuzere, M., Verhoest, N.E., Dorigo, W.A., Waegeman, W., 2017. A non-linear granger-causality framework to investigate climate–vegetation dynamics. Geosci. Model Dev. (GMD) 10, 1945–1960.
Petchiappan, A., Steele-Dunne, S.C., Vreugdenhil, M., Hahn, S., Wagner, W., Oliveira, R., 2021. The influence of vegetation water dynamics on the ascat backscatter-incidence angle relationship in the amazon. Hydrol. Earth Syst. Sci. Discuss. 1–29.
Pfeil, I., Vreugdenhil, M., Hahn, S., Wagner, W., Strauss, P., Blöschl, G., 2018. Improving the seasonal representation of ascat soil moisture and vegetation dynamics in a temperate climate. Rem. Sens. 10, 1788.
Pfeil, I., Wagner, W., Forkel, M., Dorigo, W., Vreugdenhil, M., 2020. Does ASCAT observe the spring reactivation in temperate deciduous broadleaf forests? Rem. Sens. Environ. 250, 112042.
Pierdicca, N., Fascetti, F., Pulvirenti, L., Crapolicchio, R., Muñoz-Sabater, J., 2015. Analysis of ascat, smos, in-situ and land model soil moisture as a regionalized variable over europe and north africa. Rem. Sens. Environ. 170, 280–289.
Quast, R., Wagner, W., 2016. Analytical solution for first-order scattering in bistatic radiative transfer interaction problems of layered media. Appl. Opt. 55, 5379–5386.
Saatchi, S., Halligan, K., Despain, D.G., Crabtree, R.L., 2007. Estimation of forest fuel load from radar remote sensing. IEEE Trans. Geosci. Rem. Sens. 45, 1726–1740.
Santoro, M., Beaudoin, A., Beer, C., Cartus, O., Fransson, J.E., Hall, R.J., Pathe, C., Schmullius, C., Schepaschenko, D., Shvidenko, A., Thurner, M., Wegmüller, U., 2015. Forest growing stock volume of the northern hemisphere: spatially explicit estimates for 2010 derived from envisat asar. Rem. Sens. Environ. 168, 316–334.
Seneviratne, S.I., Corti, T., Davin, E.L., Hirschi, M., Jaeger, E.B., Lehner, I., Orlowsky, B., Teuling, A.J., 2010. Investigating soil moisture–climate interactions in a changing climate: a review. Earth Sci. Rev. 99, 125–161.
Steele-Dunne, S.C., Hahn, S., Wagner, W., Vreugdenhil, M., 2019. Investigating vegetation water dynamics and drought using metop ascat over the north american grasslands. Rem. Sens. Environ. 224, 219–235.
Steele-Dunne, S.C., Hahn, S., Wagner, W., Vreugdenhil, M., 2021. Towards including dynamic vegetation parameters in the eumetsat h saf ascat soil moisture products. Rem. Sens. 13, 1463.
Teubner, I.E., Forkel, M., Jung, M., Liu, Y.Y., Miralles, D.G., Parinussa, R., van der Schalie, R., Vreugdenhil, M., Schwalm, C.R., Tramontana, G., Camps-Valls, G., Dorigo, W.A., 2018. Assessing the relationship between microwave vegetation optical depth and gross primary production. Int. J. Appl. Earth Obs. Geoinf. 65, 79–91.
Ulaby, F.T., 1981. Microwave Remote Sensing, Active and Passive.
Vermunt, P.C., Khabbazan, S., Steele-Dunne, S.C., Judge, J., Monsivais-Huertero, A., Guerriero, L., Liu, P.-W., 2021. Response of subdaily l-band backscatter to internal and surface canopy water dynamics. IEEE Trans. Geosci. Rem. Sens. 59, 7322–7337.
Vreugdenhil, M., Dorigo, W.A., Wagner, W., De Jeu, R.A., Hahn, S., Van Marle, M.J., 2016. Analyzing the vegetation parameterization in the TU-wien ASCAT soil moisture retrieval. IEEE Trans. Geosci. Rem. Sens. 54, 3513–3531.
Wagner, W., Lemoine, G., Borgeaud, M., Rott, H., 1999a. A study of vegetation cover effects on ers scatterometer data. IEEE Trans. Geosci. Rem. Sens. 37, 938–948.
Wagner, W., Noll, J., Borgeaud, M., Rott, H., 1999b. Monitoring soil moisture over the canadian prairies with the ERS scatterometer. IEEE Trans. Geosci. Rem. Sens. 37, 206–216.
Wagner, W., Lemoine, G., Rott, H., 1999c. A method for estimating soil moisture from ers scatterometer and soil data. Rem. Sens. Environ. 70, 191–207.
Wagner, W., Hahn, S., Kidd, R., Melzer, T., Bartalis, Z., Hasenauer, S., Figa-Saldana, J., De Rosnay, P., Jann, A., Schneider, S., et al., 2013. The ASCAT Soil Moisture Product: A Review of its Specifications, Validation Results, and Emerging Applications. Meteorologische Zeitschrift.
Xu, S., Qi, Z., Li, X., Yeh, A.G.-O., 2019. Investigation of the effect of the incidence angle on land cover classification using fully polarimetric sar images. Int. J. Rem. Sens. 40, 1576–1593.